Atmospheric Research 314 (2025) 107783

Contents lists available at ScienceDirect

Atmospheric Research

journal homepage: www.elsevier.com/locate/atmosres

Impacts of land surface processes on summer extreme precipitation in Eastern China: Insights from CWRF simulations

Chenyi Zhang [a], Qingquan Li [b,c,*], Xin-Zhong Liang [d], Lili Dong [c], Bing Xie [c], Weiping Li [e,**], Chao Sun [d]

[a] *Chinese Academy of Meteorological Sciences, Beijing 100081, China*
[b] *Collaborative Innovation Center on Forecast and Evaluation of Meteorological Disasters, Nanjing University of Information Science and Technology, Nanjing 210044, China*
[c] *China Meteorological Administration Key Laboratory for Climate Prediction Studies, National Climate Centre, Beijing 100081, China*
[d] *Department of Atmospheric and Oceanic Science, University of Maryland, College Park, MD 20740, USA*
[e] *Earth System Modeling and Prediction Centre, China Meteorological Administration, Beijing 100081, China*

ARTICLE INFO

Keywords:
Extreme precipitation
Land surface processes
Soil moisture
Planetary boundary layer
Climate–weather research and forecasting model

ABSTRACT

Understanding the impacts of land surface processes on summer extreme precipitation is crucial for accurate climate predictions. This study investigated these impacts across three subregions of eastern China (North China, Central China, and South China) using the regional Climate–Weather Research and Forecasting model with two land surface parameterization schemes: the Conjunctive Surface–Subsurface Process (CSSP) scheme and the NOAH Land Surface Model (NOAH). When compared with observational and reanalysis data, both schemes were found to successfully reproduce the spatial distribution of extreme precipitation, with the CSSP scheme showing distinct advantages in simulating evapotranspiration. The influence of land surface processes on summer extreme precipitation varies among the three subregions, largely depending on soil moisture conditions. In North China, a transitional zone between arid and humid regions, soil moisture primarily influences extreme precipitation, with biases arising from difference between the lifting condensation level and the planetary boundary layer height. In Central China, where soil moisture is moderate, soil moisture and net radiation jointly influence extreme precipitation, with biases linked to the planetary boundary layer height. In South China, where soil moisture is mostly saturated during summer, net radiation dominates the variability of land surface variables, with latent heat bias leading to extreme precipitation bias. Overall, soil moisture affects extreme precipitation by altering the energy and stability of the planetary boundary layer and the lifting condensation level. These findings could inform the assessment and future improvement of models, and support the monitoring and predicting of extreme precipitation events.

1. Introduction

Over the past century, global temperatures have risen steadily owing to both combustion of fossil fuels and unsustainable energy and land use. This has led to more frequent and intense extreme weather events worldwide, posing increasing risk to natural ecosystems and human populations (*IPCC,* 2023). During 1961–2021, China experienced an increasing trend in extreme rainfall events, with notable regional variations, indicating a rising level of climate-related risk (China Meteorological Administration Climate Change Centre, 2022). Therefore, further research on the patterns of extreme precipitation holds considerable scientific value.

Extreme precipitation is difficult to simulate accurately, and understanding the physical mechanisms underlying model biases remains a challenge. General circulation models (GCMs) are essential tools used for studying climate variability and change (IPCC, 2013). Many studies have assessed the ability of GCMs to simulate the climate of China. Although GCMs have been found broadly capable of capturing the mean surface and extreme temperature distributions, substantial uncertainty remains regarding their ability to simulate precipitation characteristics

---

* Corresponding author at: Collaborative Innovation Center on Forecast and Evaluation of Meteorological Disasters, Nanjing University of Information Science and Technology, Nanjing 210044, China.

** Corresponding author.

E-mail addresses: liqq@cma.gov.cn (Q. Li), liwp@cma.gov.cn (W. Li).

https://doi.org/10.1016/j.atmosres.2024.107783
Received 26 July 2024; Received in revised form 29 October 2024; Accepted 11 November 2024

(Hu et al., 2014). For example, the Coupled Model Intercomparison Project phase 5 (CMIP5) simulations show severe wet biases in western and northern China, together with dry biases in southeastern China, thereby exhibiting marked regional variations (Chen and Frauenfeld, 2014; Jiang et al., 2015). Although the latest CMIP phase 6 (CMIP6) models generally reduce the dry biases seen in CMIP5 simulations, wet biases persist in the intensity of heavy precipitation over eastern China, particularly in the region of the mid–lower reaches of the Yangtze River (Zhu et al., 2020; Zhang et al., 2024).

In contrast to GCMs, regional climate models (RCMs) boast superior ability in unraveling regional processes owing to their refined representation of the underlying physics at higher resolution. Consequently, RCMs demonstrate great improvement in capturing regional precipitation characteristics. Previous studies that utilized a nested GCM–RCM approach to simulate temperature and precipitation demonstrated enhanced performance in downscaling both the spatial distributions and the seasonal variations of extreme temperature and extreme precipitation in China, thereby elucidating more regional-scale features (Zou and Zhou, 2013; Wei et al., 2019). The Climate–Weather Research and Forecasting (CWRF) model, which is a new-generation RCM developed by Liang et al. (2012), has refined representation of the key physical processes in the Weather Research and Forecasting (WRF) model, and represents a remarkable advancement in the simulation of the climate of China. In comparison with other popular RCMs, the CWRF model can more realistically capture the annual cycle and the interannual variations in mean and extreme precipitation, and the distributions of the two rain belts present in summer along the Yangtze River and over South China (Liu et al., 2008; Liang et al., 2012). Its simulation of teleconnections with large-scale circulation features is also good, which partly explains its better performance in precipitation simulation (Li et al., 2020). Jiang et al. (2021) nested the Community Climate System and CWRF models to project precipitation over China from 2018 to 2050, which indicated that the downscaling correction of the current climate simulation by the CWRF model could be applied systematically to future climate projections.

Land surface processes have crucial impact on precipitation (Koster et al., 2004; Findell et al., 2011; Wei et al., 2018). Approximately 30 % of Earth's surface has complex and heterogeneous land cover. Land surface variables such as soil moisture, soil temperature, vegetation, and snow cover regulate the fluxes of energy, water, and carbon by partitioning the available energy, thereby exerting notable influence on the climate both regionally and globally (Seneviratne et al., 2006; Zhang et al., 2011a; Wang et al., 2021; Yao et al., 2021). The Global Land–Atmosphere Coupling Experiment, which investigated the role of soil moisture in climate feedbacks in past and future climate systems, yielded two key findings: (1) marked model discrepancies in the simulation of the response of both precipitation and temperature to soil moisture variations, and (2) more pronounced impacts of soil moisture variations on precipitation and temperature in the transitional zone between arid and humid regions. Several studies highlighted the important role of the fluxes of water vapor and heat from the land surface to the atmosphere in shaping the development of the planetary boundary layer (PBL), thereby affecting precipitation and playing a critical role in land surface hydrology and atmospheric processes. Soil moisture and snow cover can alter the surface albedo and local water cycles with consequential effects on precipitation. Moreover, complex interactions also exist between vegetation and the atmosphere, whereby changes in vegetation not only modify land surface flux exchanges by adjusting the surface albedo and roughness, but also influence processes such as precipitation interception, evapotranspiration, and soil infiltration, thereby affecting the water cycle and subsequently influencing precipitation. Additionally, the subsurface soil temperature, owing to its prolonged memory, holds considerable potential value for summer climate prediction (Hirschi et al., 2011; Seneviratne et al., 2010; Miralles et al., 2012; Hagemann et al., 2016; Hauser et al., 2017). In conclusion, land–atmosphere interaction has become recognized as an indispensable component in climate research, representing a frontier topic of current interdisciplinary concern (Findell et al., 2017; Findell et al., 2023; Findell et al., 2024; Li et al., 2018; Chen et al., 2019; Qiao et al., 2023; Yang et al., 2023).

Research using the CWRF model to simulate regional extreme precipitation over China is lacking, particularly with regard to the influence of land surface processes on extreme precipitation. Hence, the objectives of this study were to assess the skill of the CWRF model in simulating extreme precipitation over China using different land surface schemes, and to further explore the impacts of land surface processes on extreme precipitation over China and the related physical mechanisms.

2. Model, data, and methods

2.1. Model

The CWRF model used in this study is a climate extension of the WRF model, but with marked improvement in the parameterization of physical processes compared with that of the WRF model (Liang et al., 2012). The improvements involve land–atmosphere–ocean interactions, convection–microphysics interactions, and cloud–aerosol–radiation interactions. The CWRF model also integrates optional parameterization schemes for ocean, PBL, cumulus, microphysics, cloud, aerosol, and radiation processes, which are coupled across all components to ensure maximum consistency throughout the model (Liang et al., 2012).

Of particular relevance to this study, the CWRF model incorporated two land surface parameterization schemes, the Conjunctive Surface–Subsurface Process (CSSP) scheme and the NOAH Land Surface Model (NOAH) scheme, which were used to predict the distributions of soil temperature and moisture, land hydrological changes, and land–atmosphere flux exchanges. The CSSP scheme divides the soil into 11 layers and employs a three-dimensional volume-averaged soil moisture transport model, incorporating lateral flow and subgrid heterogeneity induced by topographic features. It handles surface and subsurface runoff using dynamic prediction to produce more reasonable variations in the saturated zone depth. The CSSP scheme serves as the core land surface scheme (Choi et al., 2006; Choi et al., 2007; Choi et al., 2013; Yuan and Liang, 2011). The NOAH scheme divides the soil into 4 layers and employs a Richard's equation derived under the assumptions of rigidity, isotropy, and one-dimensional vertical flow. Simultaneously, it regulates surface and subsurface runoff employing equilibrium approximation (Ek and Mahrt, 1991; Ek et al., 2003; Chen and Dudhia, 2001; Niu et al., 2011). Further details are provided in Table S1.

The computational domain of the CWRF model adopted in this study was centered at 35.18°N, 110°E on the Lambert conformal map projection, with grid spacing of 30 km, encompassing 171 (longitude) × 231 (latitude) grid points (Fig. S1). There were 36 vertical layers, with the top-layer pressure set at 50 hPa. Liu et al. (2008) demonstrated that this computational domain is optimal for regional climate modeling in China, yielding better performance in terms of statistical errors, correlations, and mean precipitation.

2.2. Data

In this study, the CWRF simulations were driven by ERA-I reanalysis dataset (Dee et al., 2011) as the initial and boundary conditions. The horizontal resolution of ERA-I data is 0.75°longitude by 0.75°latitude. Each CWRF simulation was initialized on October 1, 1979 and integrated continuously through to December 31, 2016 with 6-hourly lateral boundary forcing and daily sea surface temperature variation from ERA-I. No additional data assimilation or nudging within the CWRF computational domain was included. The initial 3 months were considered as a spin-up and were not used in the subsequent analyses. The simulation results from 1982 to 2016 (totaling 35 years) were used in this study. Given that summer exhibits the most pronounced land–atmosphere coupling in East Asia, our primary assessment period focused on summer (June–July–August) during 1982–2016.

We used the CN05.1 dataset of daily precipitation and temperature at 2-m height (T_{2m}) over China as reference for model evaluation. The CN05.1 gridded dataset is generated through interpolation of observations recorded since 1961 at 2416 stations distributed across mainland China, boasting resolution of 0.25° × 0.25°. This dataset is used widely in investigations of extreme precipitation throughout China (Wu and Gao, 2013; Liang et al., 2018). Daily data of soil moisture and evapotranspiration were sourced from the ERA5-Land reanalysis dataset (Muñoz-Sabater et al., 2021), with resolution of 0.1° × 0.1°. Soil moisture was defined as the surface layer, i.e., 0–10 cm. Additionally, daily data of sensible heat, latent heat, PBL height (PBLH), and radiation data were extracted from the ERA5 reanalysis dataset (Hersbach et al., 2020), with resolution of 0.25° × 0.25°. For convenience of comparison, the CN05.1 data and reanalysis data were interpolated to the model's horizontal resolution of 30 km. Although this interpolation might have induced minor biases, these biases were considered negligible (Sun and Liang, 2020a, 2020b).

2.3. Methods

Owing to the effects of the geographical environment and the monsoon, the variation in extreme precipitation over China exhibits remarkable regional differences. Eastern China, which is the primary area for summer precipitation, is characterized by a dense network of observation stations; therefore, we paid special attention to the occurrence of extreme precipitation in eastern China. Following the division of different terrain heights over China (Liang et al., 2018), three key subregions in eastern China were identified: North China (NC), Central China (CC), and South China (SC), as shown in Fig. 1. The names of the specific regions mentioned in this paper are marked with red bold fonts in Fig. S2.

Based on the definitions from the Expert Team on Climate Change Detection and Indices (Frich et al., 2002; Zhang et al., 2011b), this study adopted three extreme precipitation indices: R95p, R10, and P95. In particular, we focused on P95, which is defined as the 95th percentile of wet days (defined as daily precipitation ≥1 mm/d), consistent with Sun and Liang (2020b). The R95p and R10 indices were considered to validate the reliability of the P95 simulations. Table 1 lists the definitions of these indices. The ERA5 and CWRF model outputs do not include the lifting condensation level (LCL) and moist static energy (MSE), the definitions for these parameters are presented as Eqs. (1) and (2), with the definition of LCL adopted from Wei et al. (2021):

Table 1
Definitions of extreme precipitation indices.

Label	Index Definition	Index Unit
P95	95th percentile of wet days	mm/d
R95p	Summer annual total precipitation when daily precipitation amount on a wet day is > P95	mm
R10	Summer annual count of days when precipitation is ≥10 mm	d

$$Z_{LCL} \approx 125 \times (T_{2m} - T_d) \tag{1}$$

where T_{2m} is air temperature at 2-m height (unit: °C), and T_d is the dew point temperature (unit: °C). The unit of Z_{LCL} is meter.

$$MSE = C_pT + Lq + gz \tag{2}$$

where C_p is the specific heat capacity at constant pressure (unit: J/(Kg·K)), T is temperature on the absolute scale (unit: K), L is latent heat (unit: W/m^2), q is specific humidity (unit: Kg/Kg), and z is height (unit: m). The unit of MSE is Joules per kilogram.

To quantify the relative contributions of land surface variables to extreme precipitation and to resolve the problem of multicollinearity, we employed the open-source 'lavvan' software on the 'R' platform to construct a Structural Equation Model (SEM) for assessment of the simulation. This method was introduced for climatic diagnosis of extreme precipitation by Sun and Liang (2020b). All parameter settings were configured by adopting default algorithms, including the maximum likelihood estimation. The SEM comprises manifest and latent variables, and it can test hypotheses of causal relationships between variables based on prior theories and researches. It has been proven powerful in exploring complex causal relationships between variables, largely because it does not require the normality assumption and can effectively handle non-normally distributed variables using bootstrap analysis (Finney and DiStefano, 2013; Nevitt and Hancock, 2009). Prior to constructing the SEM, all data were normalized with a zero mean and

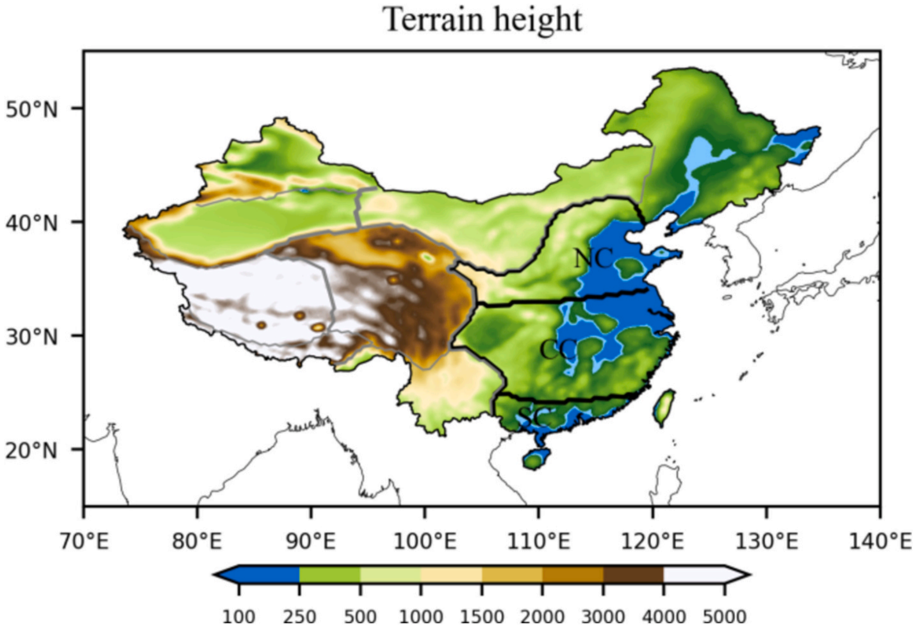

Fig. 1. Terrain height and regional division in China. Shading denotes terrain height (m). NC, CC, and SC stand for North China, Central China, and South China, respectively (from Liang et al., 2018).

unit deviation, resulting in standardized path coefficients. The final model had to meet the following conditions: (1) statistically significant path coefficients must remain consistent with the correlations; (2) the comparative fit index, one of the measures affected least by the sample size, is in the range 0.0–1.0, with values close to 1.0 indicating good fit (≥0.90 to avoid accepting a misspecified model); (3) the standardized root mean square residual has a value below 0.08, indicating good model fit (0 indicates perfect fit); and (4) the root mean square error of approximation has a value below 0.08, indicating good fit (Hu and Bentler, 1999; Hooper et al., 2008).

To assess quantitatively the similarity in the spatial distribution between the simulations and the observations, Taylor diagrams were utilized to represent the pattern correlation coefficient, standard deviation, and centered root mean square error. A higher pattern correlation coefficient, a value of the standard deviation closer to 1, and a smaller centered root mean square error indicate better model simulation performance. In comparison of the time series correlation, the temporal correlation coefficient was calculated using Pearson correlation coefficients. Furthermore, the root mean square error was employed to measure the deviations between the simulations and the observations. For the aforementioned correlation coefficients, student-*t*-tests were conducted, following a t-distribution of N-2 degrees of freedom, where N represents the sample size. The t-statistic value was calculated based on the correlation coefficients (r) of the simulations and the observations, and its absolute value was compared with the critical value from the t-distribution table at the defined significance level. If the absolute value exceeded the critical value, the correlation coefficient was considered statistically significant (Wei, 1999).

$$t = \sqrt{N-2}\,\frac{r}{\sqrt{1-r^2}} \tag{3}$$

3. Simulations of extreme precipitation with different land surface parameterization schemes

Fig. 2 presents the spatial distribution of extreme precipitation in China during summer, comparing observations with CWRF simulations using the CSSP and NOAH schemes. In terms of the mean precipitation, the observations reveal two rain belts located in the Yangtze River and SC (Fig. 2a). The simulation with the CSSP scheme closely matches the observations but tends to overestimate precipitation in southwestern China and SC, and underestimate precipitation in the middle and lower reaches of the Yangtze River (Fig. 2e). The rain belt simulated using the NOAH scheme in the Yangtze River is less distinct, and the precipitation in most regions of China is generally underestimated (Fig. 2i). The CSSP and NOAH schemes both overestimate precipitation in Northeast China, possibly because of the sparse distribution of observation stations in the mountainous regions, which could lead to underestimation of total precipitation and intensity (Liang et al., 2018). Hence, higher-resolution monitoring stations and objective terrain adjustments are needed to provide more accurate reference data for model assessments.

Observation indicates that P95 decreases from the southeast toward the northwest over China (Fig. 2b). The CSSP and NOAH schemes both capture the high-value areas of P95 effectively but tend to overestimate P95 in Northeast China and central-western China, and neither schemes captures the areas of high P95 in Chongqing City, Guizhou Provinces, and SC (Fig. 2f and j).

Similar to P95, R95p also exhibits a distribution with a southeast-to-northwest gradient (Fig. 2c). The R95p simulated by the CSSP scheme is consistent with the observations (Fig. 2g), whereas the NOAH scheme fails to reproduce the spatial distribution of R95p effectively, narrowing the overall areas of high R95p and underestimating precipitation in Chongqing City, Guizhou Province and Hunan Province (Fig. 2k).

The values of R10 gradually decrease from the south toward the north, with southwestern, southern, and southeastern China representing areas of high R10 (Fig. 2d). The CSSP and NOAH schemes both severely underestimate R10 in the middle and lower reaches of the Yangtze River, but substantially overestimate it in SC. Additionally, the CSSP scheme generates a fake center of high R10 in southwestern China (Fig. 2h and l).

Fig. 3 presents the frequency distributions and spatial distributions of extreme precipitation simulations biases. The frequency distributions are described using kernel density estimators. It can be seen that the CSSP and NOAH schemes exhibit similar bias frequencies in mean

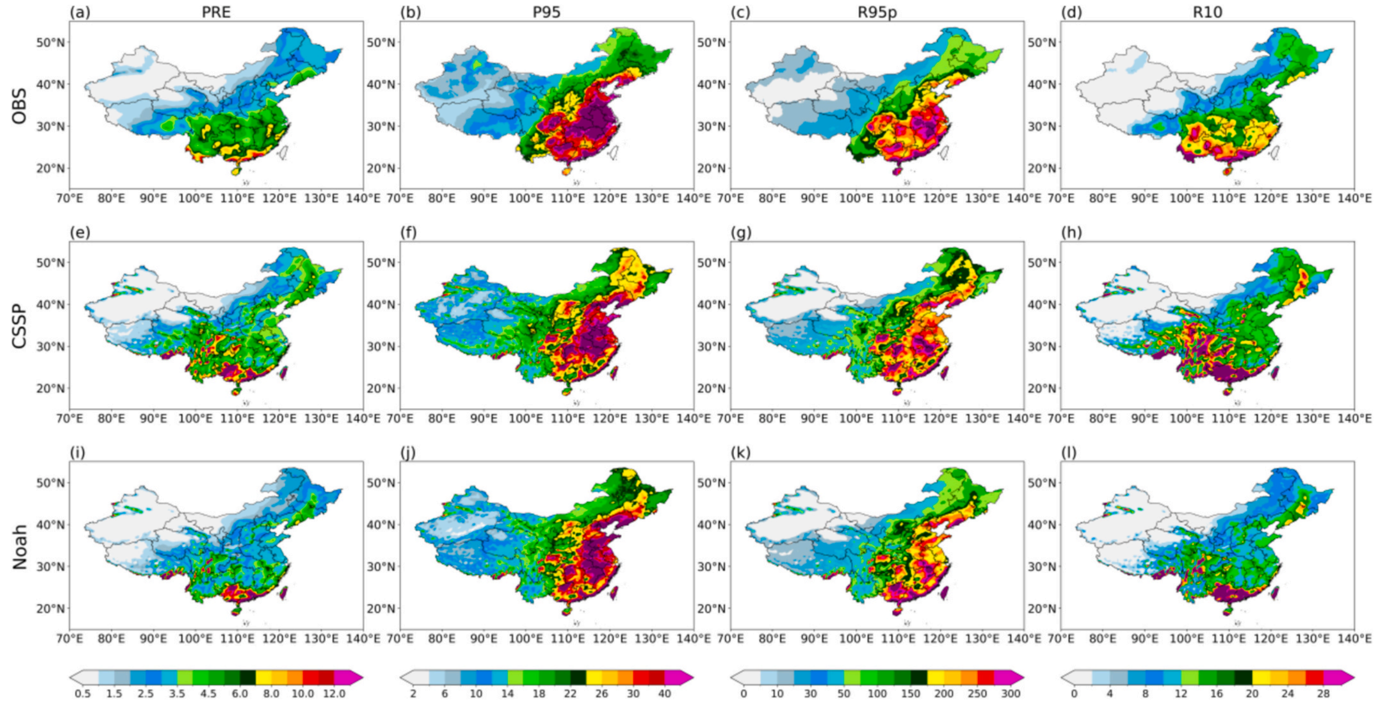

Fig. 2. (a, e, i) Spatial distributions of mean precipitation (mm/d), (b, f, j) P95 (mm/d), (c, g, k) R95p (mm) and (d, h, l) R10 (d) from the (a-d) observations, (e-h) the CSSP scheme and (i-l) the NOAH scheme simulations in summer during 1980–2016.

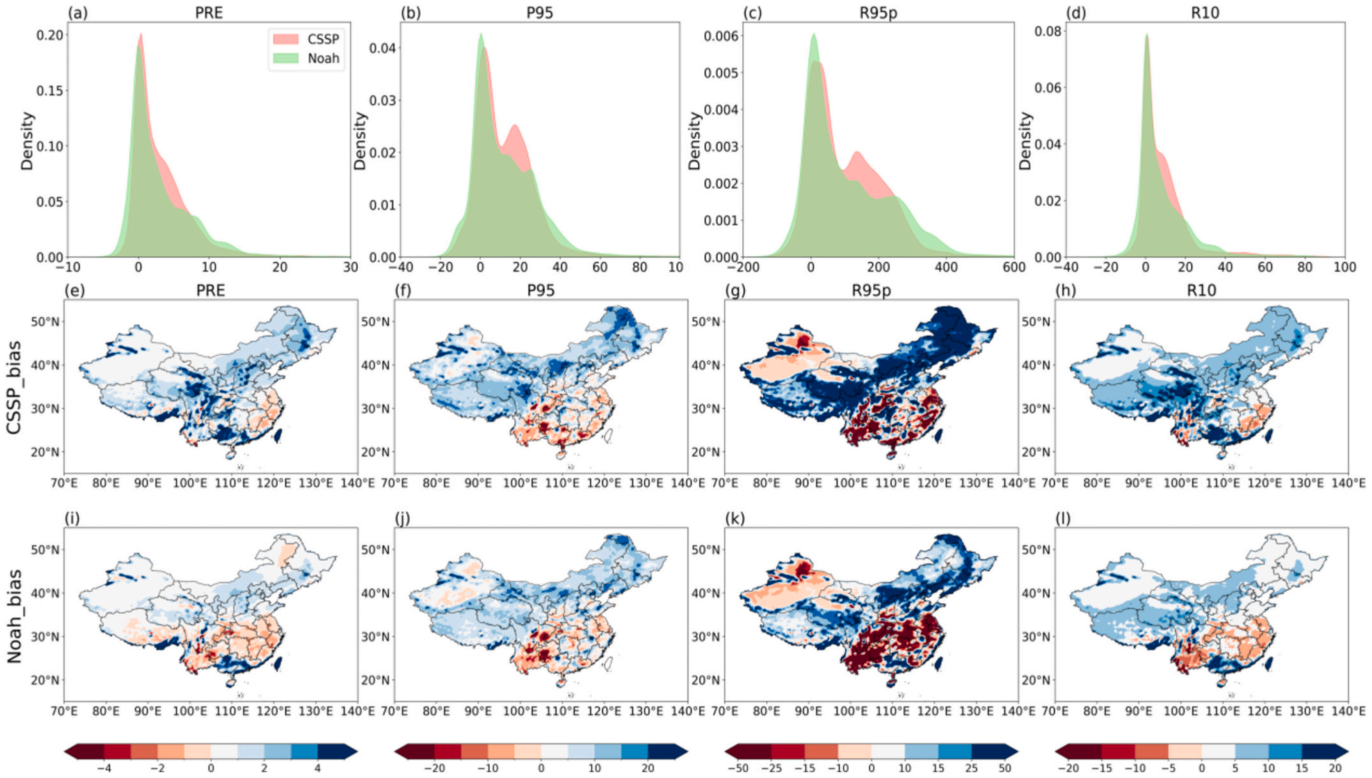

Fig. 3. (a-d) Frequency distributions and (e-i) spatial distributions of biases in (a, e, i) mean precipitation (mm/d), (b, f, j) P95 (mm/d), (c, g, k) R95p (mm) and (d, h, l) R10 (d) from (e-h) the CSSP scheme and (i-l) the NOAH scheme simulations in summer during 1980–2016.

precipitation, with peaks around the value of 0 mm/d. The NOAH scheme shows a slightly left-skewed frequency pattern, indicating a more negative (dry) bias (Fig. 3a). In terms of spatial distributions (Fig. 3e and i), notable regional variations exist between the CSSP and NOAH schemes. The CSSP scheme exhibits weak negative biases in the middle and lower reaches of the Yangtze River, whereas it shows positive biases in other regions of China (Fig. 3e). The NOAH scheme shows more pronounced negative biases compared with those of the CSSP scheme, and these are primarily evident along the southeastern edge of the Tibetan Plateau and in Yunnan Province, Sichuan Province, CC, and SC (Fig. 3i).

The P95 bias frequency simulated by the CSSP scheme exhibits a bimodal pattern, with peaks close to 0 and 20 mm/d, whereas the NOAH scheme shows only one prominent peak at 0 mm/d. This suggests that the positive biases in the CSSP scheme are greater than those in the NOAH scheme (Fig. 3b). Spatial distributions (Fig. 3f and j) reveal that the spatial patterns of the P95 simulation biases in both the CSSP and NOAH schemes are similar, with notable negative biases in P95 observed in Yunnan Province, southeastern Sichuan Province, SC, and the middle and lower reaches of the Yangtze River basin; the remaining regions of China exhibit positive biases.

The bias frequency distribution of R95p closely resembles that of P95, with the CSSP scheme displaying a bimodal pattern peaking at around 0 and 150 mm, whereas the NOAH scheme shows peaks at around 0 and 250 mm, although the bimodal pattern is considered atypical. At around 150 mm, the CSSP scheme shows notably higher probability density estimations compared with those of the NOAH scheme, indicating more pronounced positive biases (Fig. 3c). As shown in Fig. 3g and k, the CSSP and NOAH schemes both have notable negative biases in Yunnan Provinces and Sichuan Province, SC, and CC, with weaker negative biases in the northwestern Xinjiang Uygur Autonomous Region; the remaining regions of China show positive biases. Moreover, the CSSP scheme demonstrates more evident positive biases compared with the NOAH scheme.

The CSSP and NOAH schemes both show similar R10 bias frequency distributions, with narrow peaks at around 0 d (Fig. 3d). Regarding the spatial distributions (Fig. 3h and l), the CSSP scheme exhibits weak negative biases in CC and positive biases across the remainder of China. The NOAH scheme generates broader areas and intensities of negative biases compared with the CSSP scheme, with negative biases occurring in Yunnan Province, the middle and lower reaches of the Yangtze River basin, and Northeast China; the remaining regions of China exhibit positive biases.

Fig. 4 presents Taylor diagrams of the pattern correlation coefficient for extreme precipitation in three subregions: NC, CC, and SC. The azimuth indicates the pattern correlation coefficient between the observations and the simulations, and the polar radius indicates the standard deviation of the observations and the simulations. Overall, the CSSP scheme outperforms the NOAH scheme in simulating both mean precipitation and R10, exhibiting higher correlation coefficients and lower standard deviations. For P95 and R95p, in NC and CC, the simulations of the CSSP and NOAH schemes are comparable, but the NOAH scheme demonstrates superior simulation performances for P95 in NC, exhibiting lower standard deviations. In SC, the simulations of the CSSP and NOAH schemes are relatively poor, possibly owing to the complex mechanisms regulating precipitation in SC, as indicated by previous studies (Zhang et al., 2017, 2018; Gu et al., 2018; Xue et al., 2022).

Fig. 5 illustrates the temporal correlation coefficients and root mean square errors for extreme precipitation across the three subregions. For mean precipitation, the NOAH scheme excels in capturing the temporal evolution trend in NC, outperforming the CSSP scheme with a higher temporal correlation coefficient and a lower root mean square error. In contrast, the CSSP scheme demonstrates superior capability in CC and SC, exhibiting higher temporal correlation coefficients compared with those of the NOAH scheme. However, the CSSP scheme also produces a higher root mean square error in SC owing to its tendency to overestimate mean precipitation (Fig. 3a and e). Notably, the NOAH scheme fails to accurately capture the temporal evolution trend in SC. Regarding

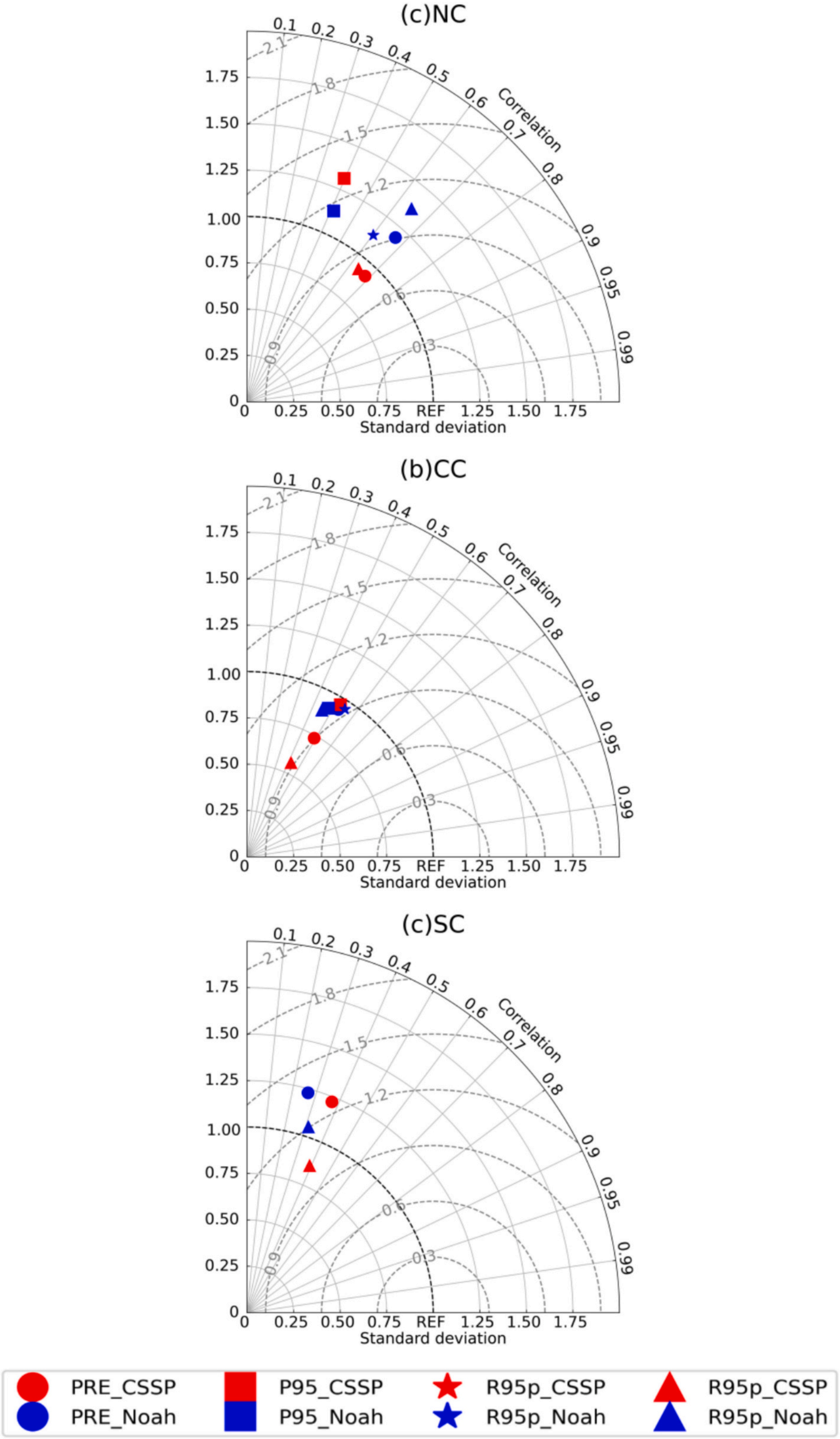

Fig. 4. Taylor diagrams of the pattern correlation coefficient for extreme precipitation in (a) North China (NC), (b) Central China (CC), and (c) South China (SC) from the CSSP and NOAH scheme simulations in summer. Circles, squares, stars, and triangles indicate mean precipitation (mm/d), P95 (mm/d), R95p (mm), and R10 (d), respectively. Red and blue colors represent the CSSP scheme and the NOAH scheme, respectively. (For interpretation of the references to colour in this figure legend, the reader is referred to the web version of this article.)

P95, neither the CSSP scheme nor the NOAH scheme successfully captures the temporal evolution trend in NC. In CC, the CSSP scheme outperforms the NOAH scheme, exhibiting a higher temporal correlation coefficient and a lower root mean square error. The CSSP and NOAH schemes show comparable performance in SC, yet both yield a large root mean square error, particularly the CSSP scheme, indicating a certain degree of overestimation or underestimation of P95 (Fig. 3b, f, and j).

In terms of R95p, the CSSP and NOAH schemes are both relatively

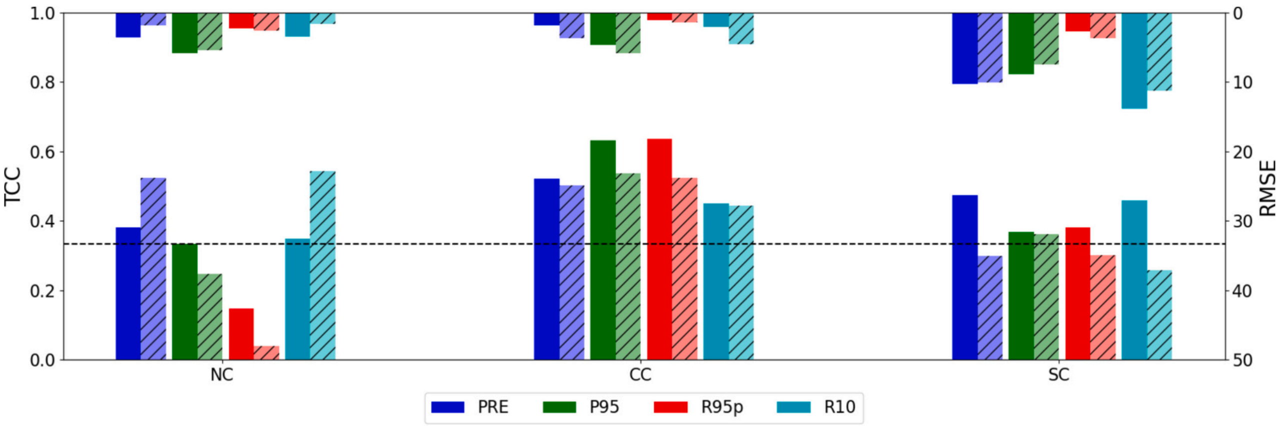

Fig. 5. Temporal correlation coefficient (TCC) and root mean square error (RMSE) of extreme precipitation in North China (NC), Central China (CC), and South China (SC) from the CSSP scheme and NOAH scheme simulations in summer during 1980–2016. Left and right y-axes represent TCC and RMSE, respectively. Dark blue, green, red, and light blue colors indicate mean precipitation (mm/d), P95 (mm/d), R95p (mm), and R10 (d), respectively. Bars with and without slashes indicate the simulations of the NOAH scheme and the CSSP scheme, respectively. Black dashed line indicates statistical significance at the 95 % confidence level in the student-*t*-test. (For interpretation of the references to colour in this figure legend, the reader is referred to the web version of this article.)

poor in NC, which might be related to their poor simulation of P95 in that region. In both SC and CC, the CSSP scheme demonstrates superior performance compared with the NOAH scheme. For example, the NOAH scheme struggles to capture the temporal evolution trend of R95p in SC and yields a lower temporal correlation coefficient and a higher root mean square error in CC. For R10, the NOAH scheme shows better simulation performance in NC, with a higher temporal correlation coefficient and a lower root mean square error. In CC, the capabilities of the CSSP and NOAH schemes are comparable. The CSSP scheme outperforms the NOAH scheme in SC, albeit with a certain degree of overestimation or underestimation that results in a relatively high root mean square error (Fig. 3d, h, and l).

Overall, we found that the spatial distribution of P95 closely resembles that of R95p, which is because P95 serves as the foundation of R95p (Fig. 2b and c). The CSSP and NOAH schemes both successfully reproduce the spatial distributions of P95 and R95p, albeit with northward shift in the high-value regions, resulting in poor simulations for SC (Fig. 2 f and j). Significant negative biases are observed in CC and SC, while positive biases are observed in NC (Fig. 3f and j). Neither scheme adequately captures R10, particularly true of the NOAH scheme (Fig. 2h and l), leading to underestimation across most areas of CC, and overestimation in NC and SC (Fig. 3h and l). Therefore, the subsequent analysis focuses on land surface processes to explore the reasons for the aforementioned biases in the three subregions.

4. Simulations of spatial distributions of soil moisture and evapotranspiration

Soil moisture affects precipitation by altering the exchange of material and energy at the land–atmosphere interface (Koster et al., 2003; Hohenegger et al., 2009; Schaefli et al., 2012; Qing et al., 2023). On one hand, soil moisture is closely linked to evapotranspiration, and variation in evapotranspiration affects both the atmospheric moisture content and the amount of water vapor transferred from the land to the atmosphere, thereby having impact on precipitation. On the other hand, soil moisture also modifies the distribution of surface energy, which alters the stability of the lower-level atmosphere and subsequently affects precipitation.

Fig. 6 depicts the spatial distributions of surface soil moisture, evapotranspiration, and their respective simulation biases. According to the ERA5-Land data, the distribution of soil moisture in China decreases gradually from the south toward the north, with high values in the east of the Tibetan Plateau and to the south of the Yangtze River, and low values in western Inner Mongolia, with NC serving as the transitional zone (Fig. 6a). The simulations of two schemes are similar, with both capturing the spatial distribution of soil moisture and showing better simulation performance in NC. In contrast to the reanalysis data, the simulations exhibit high soil moisture exclusively within SC (Fig. 6b and c). Furthermore, soil moisture biases are negative in the southeast of the Tibetan Plateau, Yunnan Province and Sichuan Province, and in SC and CC. Conversely, positive biases exist across other regions of China, with prominent occurrence in western Inner Mongolia and western parts of the Tibetan Plateau (Fig. 6g and h).

As shown by the ERA5-Land data, there is gradual reduction in evapotranspiration from the southeast toward the northwest in China. Taking a line from Yunnan Province to Jilin Province, the area on the eastern side features high evapotranspiration, and the area on the western side features transitional and low evapotranspiration, with the transitional zone predominantly spanning from the Tibetan Plateau to eastern Inner Mongolia. Evapotranspiration in the Xinjiang Uyghur Autonomous Region and western Inner Mongolia is low, with negative evapotranspiration throughout the summer, indicating that the atmosphere transfers water vapor to the land surface (Fig. 6d). In contrast to the NOAH scheme, the CSSP scheme demonstrates considerably better simulation performance, capturing the spatial distribution of evapotranspiration. Nevertheless, there is underestimation in the eastern Tibetan Plateau and the middle and lower reaches of the Yangtze River, which could possibly explain the negative biases in precipitation simulated by the CSSP scheme in SC and CC. It is also shown to overestimate evapotranspiration in eastern Inner Mongolia and northeastern China (Fig. 6e and j). The NOAH scheme fails to capture the spatial distribution in evapotranspiration, resulting in severe underestimation in most areas of China (Fig. 6f and k). On one hand, owing to the integration of vegetation and soil surface parameters in the NOAH scheme, it cannot accurately compute the related water and carbon fluxes. On the other hand, Qing et al. (2023) identified that vegetation provides the water required for evapotranspiration by accessing subsurface water. In cases where the CSSP and NOAH schemes demonstrate similar simulation performance in terms of surface soil moisture, the poor simulation of evapotranspiration by the NOAH scheme might be attributable to its treatment of the vertical distribution of soil moisture. The NOAH scheme assumes an even distribution of soil moisture in each subsurface layer, neglecting the actual geographical distribution of bedrock depth, and employs the simplest equilibrium approximation to handle surface and subsurface runoff. Owing to the lack of dynamic response, this might lead to insufficient accuracy in describing real hydrological processes, resulting in inaccurate simulation of evapotranspiration, and consequently generating more severe negative biases in simulating

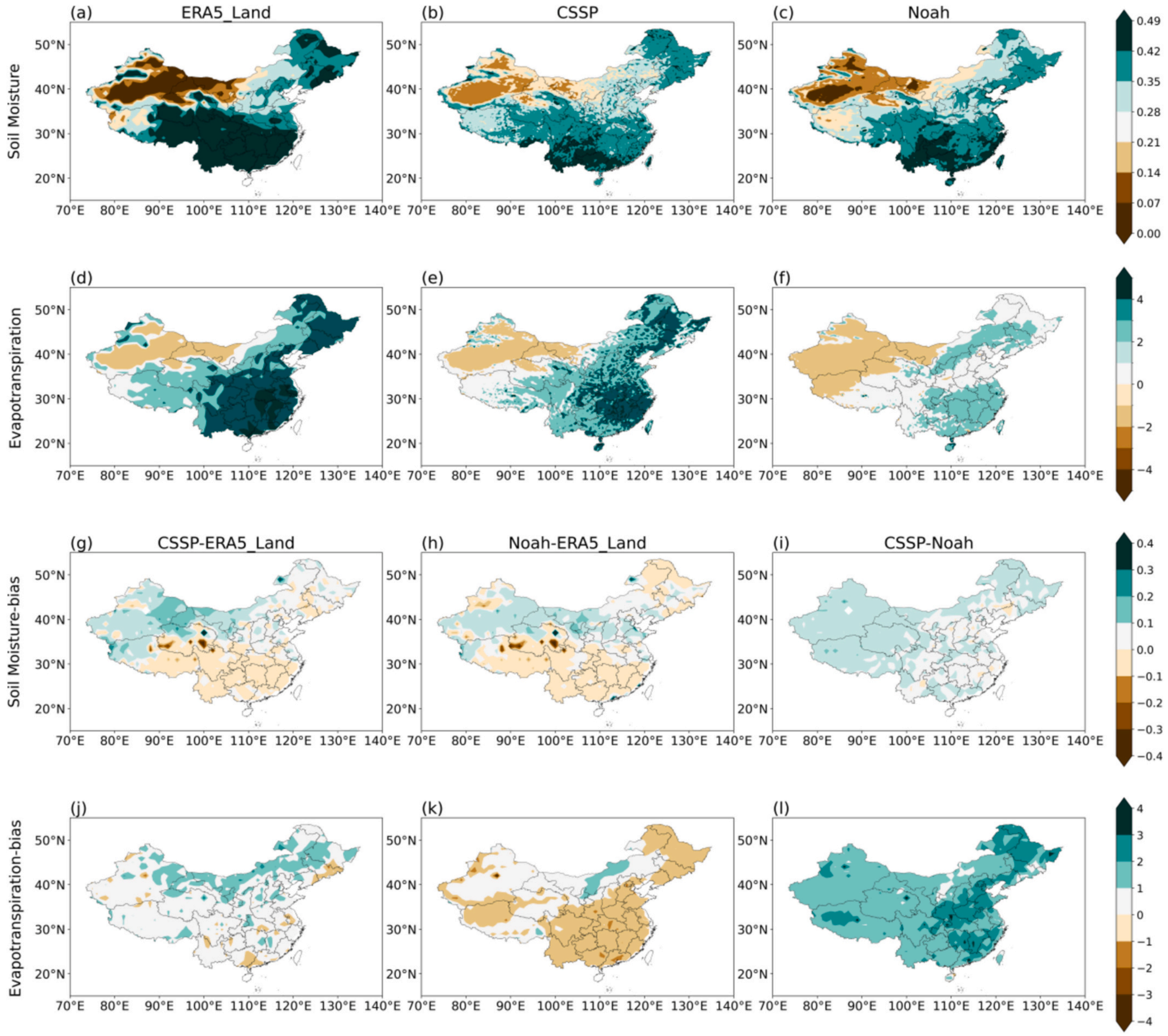

Fig. 6. (a-c) Climatological mean surface soil moisture (m^3/m^3) and (d-f) evapotranspiration (mm/d) from (a, d) ERA5-Land reanalysis, (b, e) the CSSP scheme and (c, f) the NOAH scheme simulations in summer during 1980–2016. (g, h) Soil moisture biases between the simulations and ERA5-Land reanalysis, (j, k) evapotranspiration biases between the simulations and ERA5-Land reanalysis, and (i) soil moisture bias and (l) evapotranspiration bias between the CSSP and NOAH schemes in summer.

precipitation.

In summary, compared with the NOAH scheme, the CSSP scheme demonstrates notable advantages in simulating evapotranspiration, attributable to its dynamic prediction and detailed characterization of surface and subsurface runoff changes (Choi et al., 2006; Choi et al., 2007; Choi et al., 2013; Yuan and Liang, 2011; Liang et al., 2012). Therefore, the CSSP scheme was further employed in this study to analyze the influences of land surface processes on precipitation and the related physical mechanisms.

5. Influences of land surface processes on extreme precipitation and the related physical mechanisms

The P95 index, as the foundation of R95p, is more robust and can display key features of the simulation distributions compared with R10 without being distorted by anomalies, which means that it can better reflect the characteristics of extreme precipitation (Fan et al., 1994; Karl and Knight, 1998; Frich et al., 2002). Therefore, this study employed the P95 index to investigate both the influences of land surface processes on extreme precipitation and the causes of the simulation biases in extreme precipitation. To filter out weather disturbances, we adopted the method of Wei et al. (2021) to calculate the correlation coefficients of 10-d average values for each variable in June–July–August (nine values each year). Furthermore, all correlation analysis and SEM analysis used bias values, where P95 is defined as the simulations minus the observations, and other variables are defined as the simulations minus the reanalysis values.

Previous studies revealed that the influence of soil moisture on evapotranspiration is determined largely by climatic conditions. Koster et al. (2009) summarized three ideal relationships between soil moisture and evapotranspiration: (1) when soil moisture is too low, there is insufficient water to drive evapotranspiration, resulting in zero evapotranspiration; (2) when soil moisture is too high, evapotranspiration is driven primarily by solar radiation and is not influenced by soil moisture; and (3) when soil moisture is at an intermediate level, evapotranspiration increases as soil moisture increases.

In both the ERA5-Land reanalysis data and the CSSP scheme simulations, NC is situated in a transitional zone of soil moisture, characterized by insufficient soil moisture compared with the situation in SC and CC (Fig. 6a and b). Evapotranspiration is controlled primarily by soil moisture. The correlation coefficients of the biases between the surface variables and extreme precipitation in NC, CC, and SC are shown in Fig. 7a–c, respectively, where SWDOWN represents the solar radiation received at the surface, and NSE represents the net radiation at the surface, which comprises net longwave radiation and net shortwave radiation. The definitions of other variables are listed in Table S2. It is evident from Fig. 7a that soil moisture bias is correlated positively with evapotranspiration bias, implying that as soil moisture becomes more abundant, evapotranspiration intensifies. Additionally, evapotranspiration contributes directly to precipitation by increasing the atmospheric water vapor content, and it indirectly diminishes the wet bulb temperature gradient by increasing near-surface humidity, resulting in lowering of the LCL. This favors the generation of deeper clouds, which are usually associated with greater moisture content and enhanced likelihood of convective development. When the PBLH approaches the LCL, it facilitates the triggering of convective and the development of local precipitation (Santanello et al., 2011). The mechanisms via which PBLH influences precipitation are complex. For example, intense warming can elevate the top of the PBL to the LCL, thus triggering convection and causing increased precipitation. Conversely, reduction in the magnitude of MSE per unit mass of air within the PBL can suppress cloud evolution, leading to reduced precipitation. The two interactions rely on the ambient environmental conditions. Under moist soil conditions, PBL development is greatly restricted and its top cannot reach the LCL, which mainly causes reduced precipitation by decreasing the magnitude of MSE per unit mass of air in the PBL. Under dry soil conditions, PBL development is sufficient to offset the rise in the LCL because of the decrease in low-level humidity, which triggers convection and causes increased precipitation (Eltahir, 1998; Findell and Eltahir, 2003; Santanello et al., 2011). Therefore, in NC, where soil moisture is insufficient, the PBLH and LCL jointly influence precipitation.

Although CC is characterized by abundant soil moisture in the ERA5-Land data, it is underestimated in the simulations by the CSSP scheme, placing it between NC and SC in terms of magnitude (Fig. 6a and b). Therefore, in the bias correlation analysis, evapotranspiration in CC is not only controlled by soil moisture, but also constrained to some extent by the capacity of the atmosphere to absorb water vapor. Thus, it is controlled by atmospheric conditions, primarily net radiation, as proven by the positive correlation between net radiation bias and soil moisture bias (Fig. 7b). On one hand, soil moisture could tend to enhance net shortwave radiation at the surface by reducing the surface albedo. On the other hand, the greenhouse effect associated with atmospheric water vapor could lead to greater emission of downward longwave radiation, resulting in reduction in outgoing longwave radiation from the surface (Stefan–Boltzmann Law), thereby enhancing net radiation, heating the surface, promoting evapotranspiration, and favoring the generation of clouds and precipitation. Net radiation bias also shows positive correlation with both sensible heat bias (0.78) and latent heat bias (0.92), implying that increase in net radiation leads to greater heat flux (the sum of sensible heat and latent heat) entering the PBL from the surface. With enhancement of sensible heat, turbulent mixing is also strengthened, promoting PBL development (0.96). Under relatively moist soil conditions, reduction in the magnitude of MSE per unit mass of air within the PBL has negative impact on precipitation.

In our simulations using the CSSP scheme, SC emerges with the highest soil moisture, which is at a level sufficient to satisfy atmospheric moisture demands (Fig. 6b). Evapotranspiration is controlled predominantly by atmospheric conditions (net radiation) with minimal influence

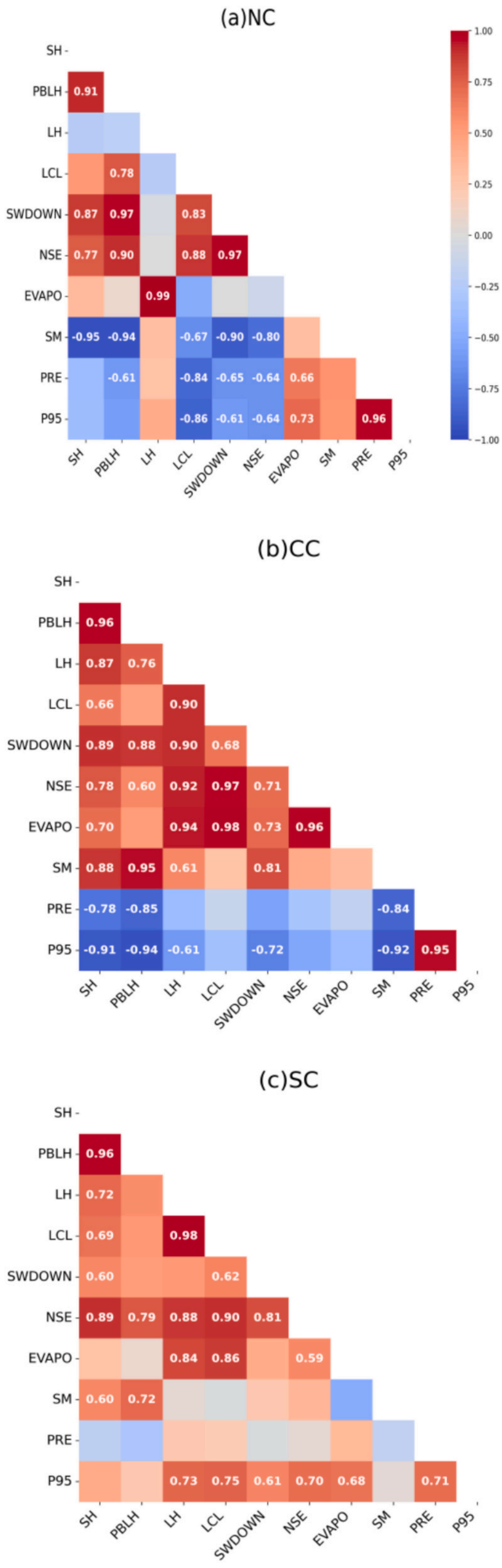

Fig. 7. Temporal correlation coefficients between surface variable biases and P95 biases from the CSSP scheme simulations averaged in (a) North China (NC), (b) Central China (CC), and (c) South China (SC) in summer during 1982–2016. Red and blue colors represent positive and negative correlation of biases, respectively. Numbers indicate correlation coefficients passing the significance test at the 90 % confidence level. (For interpretation of the references to colour in this figure legend, the reader is referred to the web version of this article.)

from soil moisture. This partially explains why areas with maximum soil moisture do not coincide with those experiencing peak evapotranspiration (Fig. 6b and e). As depicted in Fig. 7c, soil moisture bias exhibits negative correlation with evapotranspiration bias and positive correlation with net radiation bias, and net radiation bias exhibits strong positive correlation with evapotranspiration bias (0.59), whereas evapotranspiration bias shows significant positive correlation with P95 bias (0.68). It suggests that evapotranspiration in SC is less sensitive to soil moisture but more sensitive to net radiation (Dirmeyer, 2011). Enhanced net radiation heats the surface, thereby enhancing evapotranspiration and providing conditions more favorable for precipitation. Additionally, net radiation bias consistently exhibits positive correlation with sensible heat bias (0.89) and latent heat bias (0.88), indicating greater heat flux entering the PBL. Enhancement of sensible heat leads to PBL uplift (0.96), which negatively affects precipitation by reducing the magnitude of MSE per unit mass of air within the PBL. This trend is similar to that observed in CC.

It is noteworthy that evapotranspiration bias is correlated positively with LCL bias in both CC (0.98) and SC (0.86). Because evapotranspiration in these areas is controlled primarily by net radiation, and net longwave radiation is closely related to cloud properties or the LCL, it mainly reflects the influence of the LCL on evapotranspiration. Thus, the

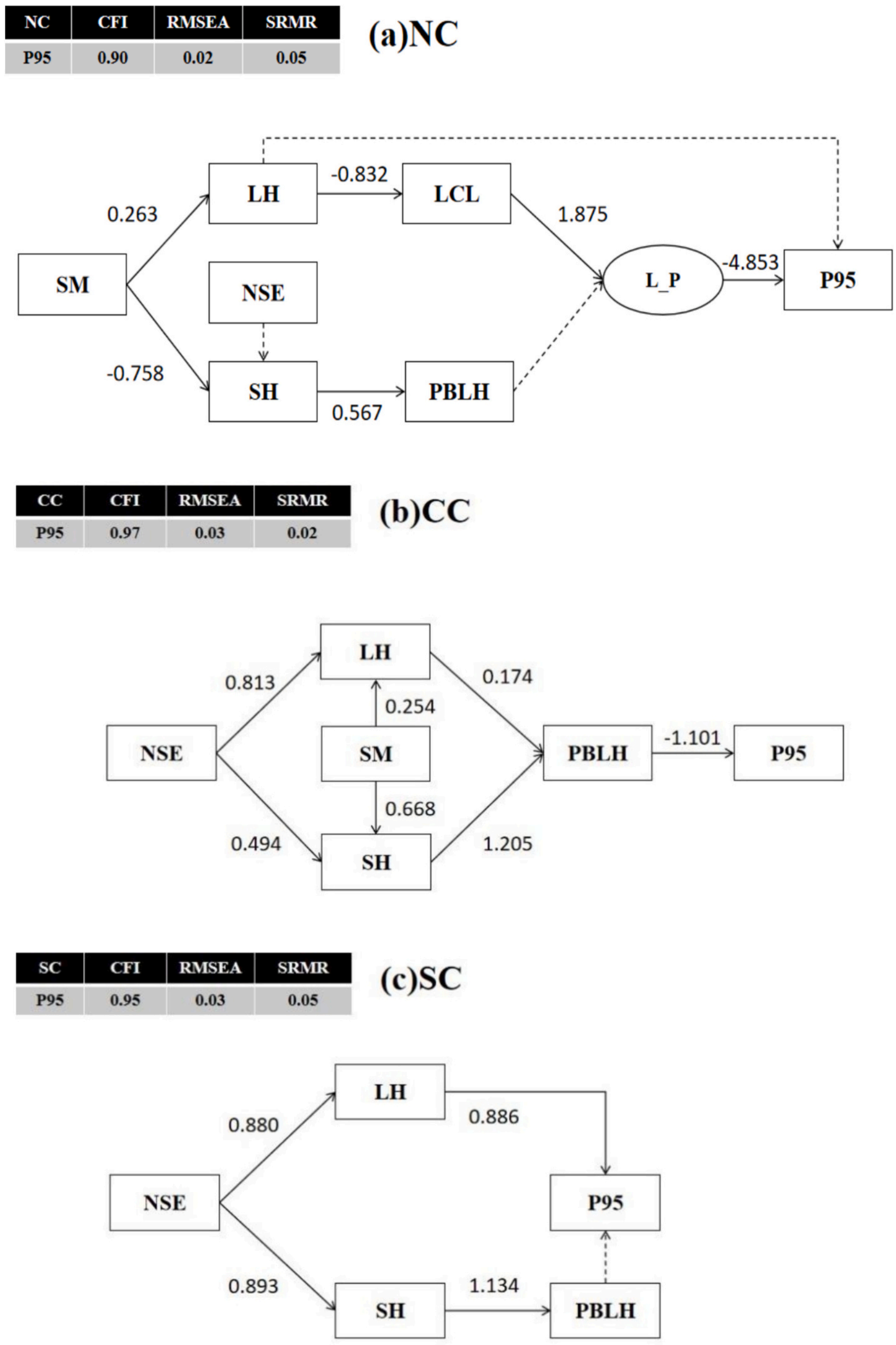

Fig. 8. Mechanisms of land surface processes influencing P95 revealed by the CSSP scheme simulations in (a) North China (NC), (b) Central China (CC), and (c) South China (SC) in summer. Rectangles and ovals represent manifest and latent variables, respectively. Solid lines indicate correlation coefficients passing the significance test at the 90 % confidence level, with numbers on the lines representing the path coefficients. CFI, RMSEA, and SRMR denote comparative fit index, root mean square error of approximation, and standardized root mean square residual, respectively.

positive relationship among LCL, net radiation, and evapotranspiration constitutes a causal chain. In contrast, in NC, soil moisture directly affects evapotranspiration, which further influences the LCL, highlighting the impact of the former on the latter (Wei et al., 2021).

The impacts of land surface processes on P95 exhibit large uncertainty, which depends not only on the climatic conditions, but also on the positive and negative feedbacks of various parameters within a region. To quantify the relative contributions of different factors to P95 in different regions, and to facilitate model improvement in future research, we constructed the SEM for further analysis. Owing to the high multicollinearity between latent heat and evapotranspiration (Fig. 7), and because latent heat almost entirely reflects the variation in evapotranspiration, only latent heat was considered to simplify the model and avoid multicollinearity.

Fig. 8 shows the mechanisms of land surface variables influencing P95 based on the SEM for three subregions. Solid lines indicate correlation coefficients passing the significance test at the 90 % confidence level, and the values on the solid lines represent path coefficients, which denote how changes in one variable affect changes in another. In NC, latent heat bias and sensible heat bias are both sensitive to soil moisture bias (0.263 and − 0.758, respectively), subsequently altering the LCL by modifying the low-level atmospheric humidity (−0.832). Introducing the latent variable L_P, inferred from manifest variables LCL and PBLH, can more directly describe the impact on precipitation. The P95 bias is affected only by L_P bias (−4.853), indicating that overestimation of precipitation occurs when the model underestimates the LCL and overestimates the PBLH. In the simulations with the CSSP scheme, notable overestimation of sensible heat spans the entire region of NC (Fig. 9f), contributing relatively by 0.567 to the PBLH biases and thereby elevating the PBLH over the entire area of NC (Fig. 9r). Simultaneously, overestimation of latent heat in the northern part of NC also leads to increased low-level atmospheric humidity, causing reduction in the LCL (Fig. 9u), and consequently contributing to reduction in L_P, which favors precipitation development. These are aligned harmoniously with the distribution of P95 simulation bias (Fig. 3f), indicating that the coupling between soil moisture and P95 is strong in the transitional zone between arid and humid regions, consistent with conclusions derived from the Global Land–Atmosphere Coupling Experiment (Koster et al., 2004, 2006). Note that over the Tibetan Plateau, high elevations lead to low T_{2m} and water vapor pressure, resulting in lower dew point temperature differences. Eq. (1) may not be suitable for approximating LCL in the Tibetan Plateau. This study, with a main focus on three subregions in eastern China, ignored the elevation effect in the Tibetan Plateau.

In CC, latent heat bias and sensible heat bias are also both influenced by the soil moisture bias (0.254 and 0.668, respectively), but are beginning to be influenced by the net radiation bias (0.813 and 0.494, respectively). The bias in P95 is influenced solely by the PBLH bias (−1.101). In the simulations with the CSSP scheme, there are significant overestimation of net radiation in CC (Fig. 9c) and underestimation of soil moisture in CC (Fig. 8g), sing 30°N as a dividing line, the north of the dividing line up to the northern boundary of CC is referred to as Northern CC, while the south of the dividing line down to the southern boundary of CC is referred to as Southern CC. It can be observed that compared to sensible heat, latent heat is more sensitive to the changes in soil moisture. As one moves south, soil moisture becomes more abundant, leading to a decreasing influence of soil moisture on latent heat, while the influence of net radiation increases. Therefore, the model underestimates latent heat in Northern CC and overestimates it in Southern CC (Fig. 9i). Additionally, sensible heat is overestimated throughout the entire CC (Fig. 9f), which may be due to the significant overestimation of net radiation in the model, indicating greater heat flux from the surface into the PBL (Fig. 9l). This promotes more vigorous convection and faster growth of the PBL (Fig. 9r), weakening of the magnitude of MSE per unit mass of air within the PBL (Fig. 9o), and underestimation of P95. Nevertheless, the negative biases in MSE per unit mass of air within the PBL can only correspond to limited areas of negative biases in P95 (Fig. 3f), suggesting that P95 is influenced by a combination of factors other than simply land surface processes.

In SC, latent heat bias and sensible heat bias are both influenced only by the net radiation bias (0.880 and 0.893, respectively). The bias in P95 is influenced solely by the latent heat bias (0.886), indicating that overestimation of latent heat by the model leads to overestimation of P95. In the simulations with the CSSP scheme, the underestimation of net radiation in SC leads to underestimation of latent heat (Fig. 9i), which directly leads to the underestimation of P95. This is consistent with the distribution of the P95 simulation biases (Fig. 3f), implying that variations in local water vapor and its energy play a certain role in P95 in SC.

In summary, among the three subregions, NC, in the transitional zone between arid and humid regions, exhibits relatively robust coupling between soil moisture and P95. The crucial influence of soil moisture on P95 stems from its capacity to modify the energy and stability of the PBL and LCL, thereby influencing the triggering mechanisms that initiate P95.

6. Conclusion and discussion

This study analyzed the impact of land surface processes on the simulation of summer extreme precipitation by the regional climate model CWRF, focusing on three subregions in eastern China: NC, CC, and SC. We evaluated the performance of two land surface parameterization schemes, i.e., the CSSP and NOAH scheme, in simulating extreme precipitation during summer. Results showed that the CSSP and NOAH schemes exhibited similar simulation capabilities, closely reproducing the spatial distributions of observed extreme precipitation. They captured the position and movement of rain belts and the areas of high precipitation, albeit with some degree of overestimation or underestimation. There was no notable difference in the simulation of precipitation biases between the CSSP and NOAH schemes. In simulating P95 and R95p, both schemes exhibited negative biases in SC and CC and positive biases in NC. Nevertheless, the CSSP scheme presented reduction in negative biases in simulating mean precipitation and R10 compared with those of the NOAH scheme across the three subregions. Moreover, the CSSP scheme also demonstrated better capability in capturing the spatial distributions of both mean precipitation and R10 across the three subregions compared with that of the NOAH scheme. However, neither the CSSP scheme nor the NOAH scheme could effectively capture the spatial distributions of both P95 and R95p in SC. The NOAH scheme exhibited greater ability in depicting the temporal evolution trends of extreme precipitation in NC, whereas the CSSP scheme performed better in SC and CC. These results indicate that, although the CWRF has overall better performance when coupling the CSSP than NOAH scheme, the latter provides skill enhancement in some regions. This suggests the use of the multi-physics ensemble, including both CSSP and NOAH, to enhance the CWRF capability in predicting mean and extreme precipitation over China. Owing to model limitations and the complexity of extreme precipitation, subsequent analysis of the influence of land surface processes on extreme precipitation might be barely satisfactory.

We evaluated the performance of both scheme in simulating surface soil moisture and evapotranspiration. The CSSP and NOAH schemes both accurately depicted the distribution of surface soil moisture, especially in the transitional zone between arid and humid regions in NC. However, compared with the reanalysis data, underestimation of soil moisture in the middle and lower reaches of the Yangtze River led to the region of maximum soil moisture appearing only in SC. In terms of evapotranspiration, the CSSP scheme demonstrated superior simulation skill, closely aligning with the reanalysis data, which might be attributable to its more refined representation of the physical processes. In contrast, the NOAH scheme struggled to capture the distribution of evapotranspiration owing to its lack of dynamic response and other

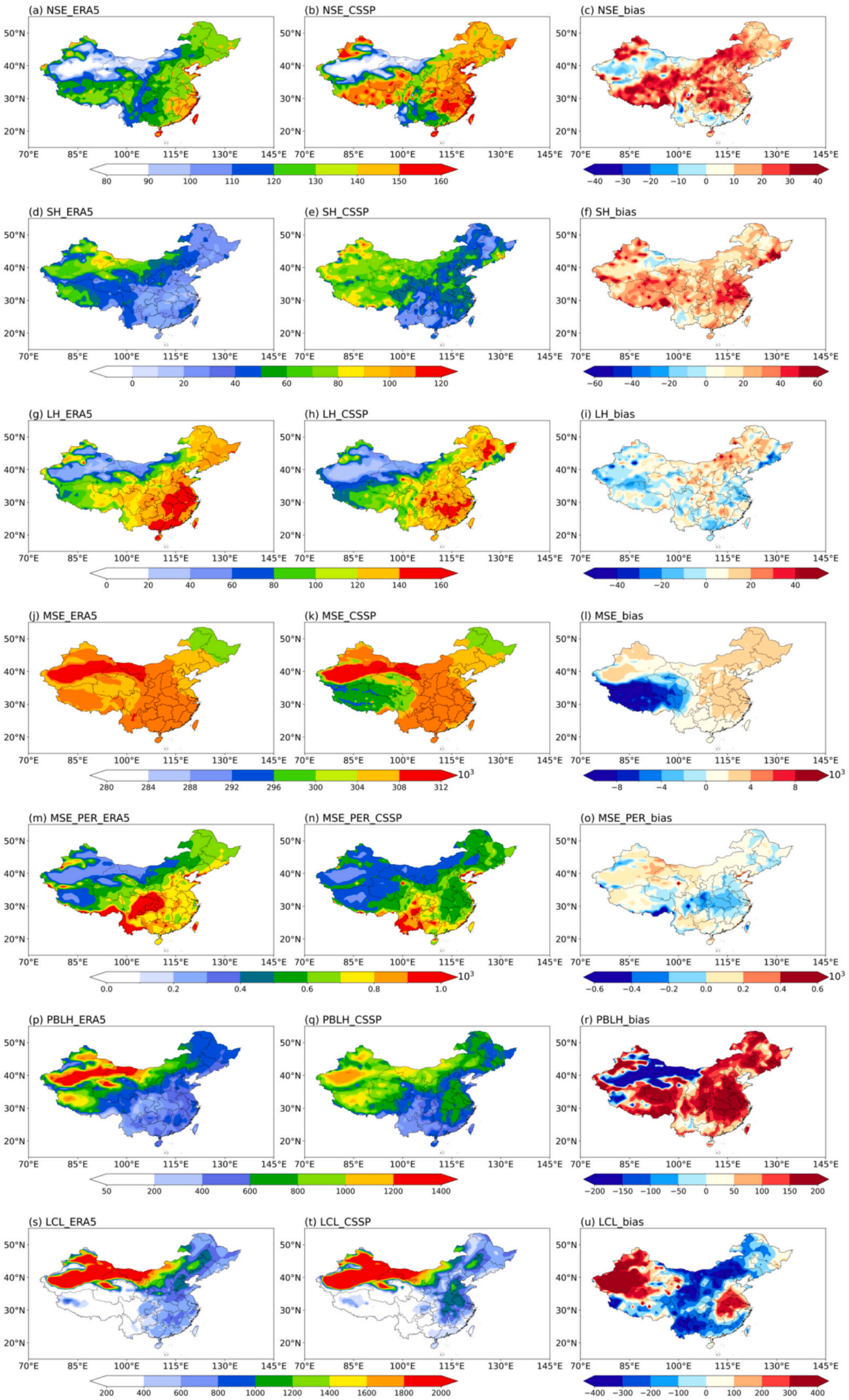
(a) NSE_ERA5 (b) NSE_CSSP (c) NSE_bias
(d) SH_ERA5 (e) SH_CSSP (f) SH_bias
(g) LH_ERA5 (h) LH_CSSP (i) LH_bias
(j) MSE_ERA5 (k) MSE_CSSP (l) MSE_bias
(m) MSE_PER_ERA5 (n) MSE_PER_CSSP (o) MSE_PER_bias
(p) PBLH_ERA5 (q) PBLH_CSSP (r) PBLH_bias
(s) LCL_ERA5 (t) LCL_CSSP (u) LCL_bias

Fig. 9. Spatial distributions of the climatological mean (a-c) NSE (W/M^2), (d-f) SH (W/M^2), (g-i) LH (W/M^2), (j-l) MSE (J/Kg), (m-o) MSE-PER (J/Kg·m), (p-r) PBLH (m), and (s-u) LCL (m), and (c, f, i, l, o, r, u) their biases between (b, e, h, k, n, q, t) the CSSP scheme simulations and (a, d, g, j, m, p, s) ERA5 reanalysis in summer during 1980–2016.

configuration limitations. This was the main reason why we selected the CSSP scheme for further research.

We investigated the potential mechanisms via which land surface processes might influence P95. First, we clarified the connection between P95 and various variables such as land surface variables, radiation variables, and the boundary layer through correlation analysis. Subsequently, we constructed a physically reasonable SEM to quantitatively measure the relative contributions of different factors. Soil moisture, net radiation, sensible heat, latent heat, PBLH, and LCL emerged as the primary influencing factors, and analysis was conducted using their bias values. Different physical mechanisms were identified as operating in the different subregions, as outlined below.

In NC, soil moisture was found to play the dominant role in influencing land surface variables. Introducing the latent variable L_P revealed that the P95 bias is influenced solely by L_P (−4.853). When L_P values are low, indicative of the close proximity of the LCL with the PBLH, convective triggering and P95 development are favored. In CC, evapotranspiration/latent heat was found to begin to show the influence of atmospheric conditions (net radiation). The P95 bias was found influenced by the PBLH bias (−1.101), indicating that PBL development inhibited P95 by reducing the magnitude of MSE per unit mass of air within the PBL. In SC, where soil moisture is abundant, net radiation exerted the dominant impact on land surface variables. The P95 bias was found influenced only by the latent heat bias (0.886), indicating that evapotranspiration enhanced atmospheric humidity, and thereby positively affected P95.

In NC, relatively strong coupling was found between soil moisture and P95, whereas in CC, the impact of land surface processes on P95 was relatively weak. In SC, P95 was found predominantly influenced by atmospheric conditions, particularly by changes in water vapor and its energy induced by net radiation. The development of extreme precipitation requires stricter demands on moisture and convective conditions, resulting from synergistic regulation by numerous factors. Compared with the large-scale circulation, land surface processes exhibit greater stability, and thus the impacts of land surface processes on extreme precipitation might be masked by large-scale circulation factors (Koster et al., 2011; Yang et al., 2015; Wei et al., 2016; Zhang et al., 2023).

The impacts of land surface processes on extreme precipitation are complex and encompass variables beyond those analyzed above. Based on previous research findings (e.g., Sun and Liang, 2020a, 2020b) and available CWRF simulations, this study takes the energy balance perspective via the lens of land–atmosphere interactions and selects the key representative variables for the in-depth SEM analysis to identify the critical physical mechanisms for extreme precipitation differences in CSSP simulations. Our analysis, however, is not complete, warranting further investigation through SEM or other machine learning approaches based on a more comprehensive list of surface and atmospheric variables. Sun and Liang (2020b) pointed out that the occurrence of P95 is influenced by the combined effects of energy supply, water supply, surface forcing, and cloud forcing. For example, deep convection can reduce outgoing longwave radiation through the re-radiation process of clouds, which can overcome the large reflected shortwave radiation at the top of atmosphere based on radiative balance, resulting in a reduced cloud radiative effect and a net warming effect to the Earth. Thus, underestimating deep convection can lead to a reduction in extreme precipitation. Additionally, the total precipitable water, in conjunction with meridional winds or upward motion, plays a regulatory role on P95, highlighting the importance of cloud microphysical processes in simulating extreme precipitation, especially in inland areas that are more dependent on water supply. Furthermore, T_{2m} can also influence P95 by affecting total precipitable water, the fraction of low layers and high layers cloud cover, and CAPE values. Our study did not include a comprehensive list of the key atmospheric variables except for PBLH and LCL that are directly related to land–convection–precipitation coupling. The lack of data for the other “causal ingredient” variables listed in Sun and Liang (2020b) limited our explanation of the full coupling mechanisms underlying the surface–atmosphere interactions affecting extreme precipitation. This remains one of our future research goals.

Furthermore, Hohenegger et al. (2009) identified differences in the land surface processes simulated by models when using different resolutions. In simulations with 25-km resolution, soil moisture and precipitation exhibit strong positive feedback, whereas in simulations with 2.2-km resolution, soil moisture and precipitation show strong negative feedback and produce different signals. Regional climate model downscaling has often been made with grid nesting at a ratio of 3:1 (Liang et al., 2001, 2005). The choice for the ratio, however, is subjective and can be relaxed to a wide range of values (Liang et al., 2019). This study conducted long-term CWRF simulations at 30-km grids, with a nesting ratio of approximate 1 (Liang et al., 2018), emphasizing the importance of model physics enhancement. Zhao and Liang (2024) compared CWRF's downscaling ability at 30, 15, and 10 km grids to determine the resolution sensitivity for extreme precipitation in year 2003. They found that the simulations at 15-km generally outperform those at 30-km across the Yangtze River Basin. Conversely, the 10-km simulation shows a consistent decline in performance compared to the 15-km run. With the improving computer resources, CWRF based operational climate forecasts has since been upgraded to 15-km in China. Nonetheless, our results from this study using 30-km CWRF provide a baseline understanding of the impact of land-atmosphere interactions on extreme precipitation prediction for further improvement through multi-physics ensemble (Zhao and Liang, 2024; Zhao et al., 2024) and resolution refinement.

CRediT authorship contribution statement

Chenyi Zhang: Writing – review & editing, Writing – original draft, Software, Formal analysis, Conceptualization. **Qingquan Li:** Writing – review & editing, Supervision, Funding acquisition, Conceptualization. **Xin-Zhong Liang:** Writing – review & editing, Methodology, Conceptualization. **Lili Dong:** Resources, Methodology, Conceptualization. **Bing Xie:** Resources, Methodology, Conceptualization. **Weiping Li:** Writing – review & editing, Supervision, Conceptualization. **Chao Sun:** Resources, Methodology.

Declaration of competing interest

The authors declare that they have no known competing financial interests or personal relationships that could have appeared to influence the work reported in this paper.

Acknowledments

This work was primarily funded by the National Key Research and Development Program of China (2022YFE0136000), the National Natural Science Foundation of China (U2242207), the Second Tibetan Plateau Scientific Expedition and Research Program of China (2019QZKK0208), the Natural Science Foundation of Anhui Province of China (2208085UQ08) and the Innovative Development Special Project of the China Meteorological Administration (CXFZ2023J003). Additionally, Liang was supported by the U.S. National Science Foundation Innovations at the Nexus of Food, Energy and Water Systems under Grant EAR1903249.

Appendix A. Supplementary data

Supplementary data to this article can be found online at https://doi.org/10.1016/j.atmosres.2024.107783.

Data availability

The authors do not have permission to share data.

References

Chen, F., Dudhia, J., 2001. Coupling an advanced land surface-hydrology model with the Penn State-NCAR MM5 modeling system. Part I: Model implementation and sensitivity. Mon. Weather Rev. 129 (4), 569–585. https://doi.org/10.1175/1520-0493(2001)129<0569:CAALSH>2.0.CO;2.

Chen, L., Frauenfeld, O.W., 2014. A comprehensive evaluation of precipitation simulations over China based on CMIP5 multi-model ensemble projections. J. Geophys. Res.-Atmos. 119 (10), 5767–5786. https://doi.org/10.1002/2013JD021190.

Chen, H., Zhan, W., Zhou, B., Teng, F., Zhang, J., Zhou, Y., 2019. Impact of nonuniform land surface warming on summer anomalous extratropical cyclone activity over East Asia. J. Geophys. Res.-Atmos. 124, 10306–10320. https://doi.org/10.1029/2018JD030165.

China Meteorological Administration Climate Change Centre, 2022. Blue Book on Climate Change of China 2022. China Meteorological New Press, Beijing.

Choi, H.I., Kumar, P., Liang, X.-Z., 2006. 3-D Volume Averaged Soil-moisture Transport Model: A Scalable Scheme for Representing Subgrid Topographic Control in Land-Atmosphere Interactions. AGU Fall Meeting Abstracts, p. 0490.

Choi, H.I., Kumar, P., Liang, X.-Z., 2007. Three-dimensional volume averaged soil moisture transport model with a scalable parameterization of subgrid topographic variability. Water Res. 43, W04414. https://doi.org/10.1029/2006WR005134.

Choi, H.I., Liang, X.-Z., Kumar, P., 2013. A conjunctive surface–subsurface flow representation for mesoscale land surface models. J. Hydrometeorol. 14, 1421–1442. https://doi.org/10.1175/JHM-D-12-0168.1.

Dee, D.P., Uppala, S.M., Simmons, A.J., Berrisford, P., Poli, P., Kobayashi, S., Andrae, U., Balmaseda, M.A., Balsamo, G., Bauer, P., Bechtold, P., Beljaars, A.C.M., van de Berg, L., Bidlot, J., Bormann, N., Delsol, C., Dragani, R., Fuentes, M., Geer, A.J., Haimberger, L., Healy, S.B., Hersbach, H., Hólm, E.V., Isaksen, L., Kallberg, P., Kohler, M., Matricardi, M., McNally, A.P., Monge-Sanz, B.M., Morcrette, J.J., Park, B.K., Peubey, C., de Rosnay, P., Tavolato, C., Thepaut, J.N., Vitart, F., 2011. The ERA-Interim reanalysis: configuration and performance of the data assimilation system. Quart. J. Meteorol. Soc. 137, 553–597. https://doi.org/10.1002/qj.828.

Dirmeyer, P.A., 2011. The terrestrial segment of soil moisture-climate coupling. Geophys. Res. Lett. 38, L16702. https://doi.org/10.1029/2011GL048268.

Ek, M.B., Mahrt, L., 1991. OSU 1-D PBL Model User's Guide. A one-dimensional planetary boundary layer model with interactive soil layers and plant canopy. Version 1.0.4. March 1991. Dept of Atmospheric Sciences, Oregon State University.

Ek, M.B., Mitchell, K.E., Lin, Y., Rogers, E., Grunmann, P., Koren, V., Gayno, G., Tarpley, D., 2003. Implementation of NOAH land surface model advances in the National Centers for Environmental Prediction operational mesoscale Eta model. J. Geophys. Res.-Atmos. 108, 8851. https://doi.org/10.1029/2002JD003296.

Eltahir, E.A.B., 1998. A soil moisture-rainfall feedback mechanism 1. Theory and observations. Water Res. 34, 765–776. https://doi.org/10.1029/97WR03499.

Fan, J., Hu, T., Truong, Y., 1994. Robust non-parametric function estimation. Scand. J. Stat. 21, 433–446. http://www.jstor.org/stable/4616328.

Findell, K.L., Eltahir, E.A.B., 2003. Atmospheric controls on soil moisture-boundary layer interactions. Part I: Framework development. J. Hydrometeorol. 4, 552–569. https://doi.org/10.1175/1525-7541(2003)004<0552:ACOSML>2.0.CO;2.

Findell, K.L., Gentine, P., Lintner, B., Kerr, C., 2011. Probability of afternoon precipitation in eastern United States and Mexico enhanced by high evaporation. Nat. Geosci. 4, 434–439. https://doi.org/10.1038/ngeo1174.

Findell, K.L., Berg, A., Gentine, P., Krasting, J.P., Lintner, B.R., Malyshev, S., Santanello Jr., J.A., Shevliakova, E., 2017. The impact of anthropogenic land use and land cover change on regional climate extremes. Nat. Commun. 8, 989. https://doi.org/10.1038/s41467-017-01038-w.

Findell, K.L., et al., 2023. Explaining and predicting Earth system change: a world climate research programme call to action. Bull. Am. Meteorol. Soc. 104 (1), E325–E339. https://doi.org/10.1175/BAMS-D-21-0280.1.

Findell, K.L., Yin, Z., Seo, E., Dirmeyer, P.A., Arnold, N.P., Chaney, N., Fowler, M.D., Huang, M., Lawrence, D.M., Ma, P., Santanello Jr., J.A., 2024. Accurate assessment of land-atmosphere coupling in climate models requires high-frequency data output. Geosci. Model Dev. 17, 1869–1883. https://doi.org/10.5194/gmd-17-1869-2024.

Finney, S.J., DiStefano, C., 2013. Nonnormal and Categorical Data in Structural Equation Modeling. Structural Equation Modeling: A Second Course, 2nd ed. IAP Information Age Publishing, pp. 439–492.

Frich, P., Alexander, L.V., Della-Marta, P.M., Gleason, B.E., Haylock, M.R., Tank, A.K., Peterson, T.C., 2002. Observed coherent changes in climatic extremes during the second half of the twentieth century. Clim. Res. 19, 193–212. https://doi.org/10.3354/CR019193.

Gu, W.L., Wang, Z., Hu, K., Hu, Y. Li, 2018. Interannual variations of the first rainy season precipitation over South China. J. Clim. 31, 623–640. https://doi.org/10.1175/JCLI-D-17-0284.1.

Hagemann, S., Blome, T., Ekici, A., Beer, C., 2016. Soil-frost-enabled soil-moisture-precipitation feedback over northern high latitudes. Earth Syst. Dynam. 7, 611–625. https://doi.org/10.5194/esd-7-611-2016.

Hauser, M., Orth, R., Seneviratne, S.I., 2017. Investigating soil moisture-climate interactions with prescribed soil moisture experiments: an assessment with the Community Earth System Model (version 1.2). Geosci. Model Dev. 10, 1665–1677. https://doi.org/10.5194/gmd-10-1665-2017.

Hersbach, H., Bell, B., Berrisford, P., Hirahara, S., Horanyi, A., Munoz-Sabater, J., Nicolas, J., Peubey, C., Radu, R., Schepers, D., Simmons, A., Soci, C., Abdalla, S., Abellan, X., Balsamo, G., Bechtold, P., Biavati, G., Bidlot, J., Bonavita, M., Chiara, G. D., Dahlgren, P., Dee, D., Diamantakis, M., Dragani, R., Flemming, J., Forbes, R.G., Fuentes, M., Geer, A.J., Haimberger, L., Healy, S.B., Hogan, R.J., Holm, E.V., Janiskova, M., Keeley, S.P., Laloyaux, P., Lopez, P., Lupu, C., Radnoti, G., Rosnay, P. D., Rozum, I., Vamborg, F., Villaume, S., Thepaut, J., 2020. The ERA5 global reanalysis. Quart. J. Roy. Meteor. Soc. 146, 1999–2049. https://doi.org/10.1002/qj.3803.

Hirschi, M., Seneviratne, S., Alexandrov, V., et al., 2011. Observational evidence for soil-moisture impact on hot extremes in southeastern Europe. Nat. Geosci. 4, 17–21. https://doi.org/10.1038/ngeo1032.

Hohenegger, C., Brockhaus, P., Bretherton, C.S., Schär, C., 2009. The soil moisture-precipitation feedback in simulations with explicit and parameterized convection. J. Clim. 22, 5003–5020. https://doi.org/10.1175/2009JCLI2604.1.

Hooper, D., Coughlan, J., Mullen, M.R., 2008. Structural equation modelling: guidelines for determining model fit. Electron. J. Bus. Res. Methods 6 (1), 53–60.

Hu, L., Bentler, P.M., 1999. Cutoff criteria for fit indexes in covariance structure analysis: conventional criteria versus new alternatives. Struct. Eq. Model. Multidiscipl. J. 6 (1), 1–55. https://doi.org/10.1080/10705519909540118.

Hu, Q., Jiang, D., Fan, G., 2014. Evaluation of CMIP5 models over the Qinghai-Tibetan Plateau. J. Atmos. Sci. (in Chinese) 38 (5), 924–938. https://doi.org/10.3878/j.issn.1006-9895.2013.13197.

IPCC, 2013. Climate change 2013: the physical science basis. In: Contribution of Working Group I to the Fifth Assessment Report of the Intergovernmental Panel on Climate Change. Cambridge University Press, p. 1535.

IPCC (Ed.), 2023. Climate Change 2023: Synthesis Report. Contribution of Working Groups I, II and III to the Sixth Assessment Report of the Intergovernmental Panel on Climate Change. IPCC, Geneva, Switzerland, pp. 35–115. https://doi.org/10.59327/IPCC/AR6-9789291691647.

Jiang, Z., Li, W., Xu, J., Li, L., 2015. Extreme precipitation indices over China in CMIP5 models. Part I: model evaluation. J. Clim. 28, 8603–8619. https://doi.org/10.1175/JCLI-D-15-0099.1.

Jiang, R., Sun, L., Sun, C., Liang, X.-Z., 2021. CWRF downscaling and understanding of China precipitation projections. Clim. Dyn. 57 (8), 1079–1096. https://doi.org/10.1007/s00382-021-05759-z.

Karl, T.R., Knight, R.W., 1998. Secular trends of precipitation amount, frequency, and intensity in the United States. Bull. Am. Meteorol. Soc. 79, 231–242. https://doi.org/10.1175/1520-0477(1998)079<0231:STOPAF>2.0.CO;2.

Koster, R.D., Suarez, M.J., Higgins, R.W., Van den Dool, H., M., 2003. Observational evidence that soil moisture variations affect precipitation. Geophys. Res. Lett. 30 (5), 1241. https://doi.org/10.1029/2002GL016571.

Koster, R.D., Dirmeyer, P.A., Guo, Z., Bonan, G.B., Chan, E., Cox, P.M., Gordon, C.T., Kanae, S., Kowalczyk, E.A., Lawrence, D.M., Liu, P., Lu, C., Malyshev, S., Mcavaney, B.J., Mitchell, K., Mocko, D.M., Oki, T., Oleson, K.W., Pitman, A.J., Sud, Y.C., Taylor, C.M., Verseghy, D.L., Vasic, R., Xue, Y., Yamada, T.J., 2004. Regions of strong coupling between soil moisture and precipitation. Science 305 (5687), 1138–1140. https://doi.org/10.1126/science.1100217.

Koster, R.D., Sud, Y.C., Guo, Z., Dirmeyer, P.A., Bonan, G., Oleson, K.W., Chan, E., Verseghy, D., Cox, P., Davies, H., Kowalczyk, E., Gordon, C.T., Kanae, S., Lawrence, D., Liu, P., Mocko, D., Lu, C., Mitchell, K., Malyshev, S., McAvaney, B., Oki, T., Yamada, T., Pitman, A., Taylor, C.M., Vasic, R., Xue, Y., 2006. GLACE: the global land-atmosphere coupling experiment. Part I: Overview. J. Hydrometeorol. 7 (4), 590–610. https://doi.org/10.1175/JHM510.1.

Koster, R.D., Schubert, S.D., Suarez, M.J., 2009. Analyzing the concurrence of meteorological droughts and warm periods, with implications for the determination of evaporative regime. J. Clim. 22, 3331–3341. https://doi.org/10.1175/2008JCLI2718.1.

Koster, R.D., Mahanama, S.P.P., Yamada, T.J., Balsamo, G., Berg, A.A., Boisserie, M., Dirmeyer, P.A., Doblas-Reyes, F.J., Drewitt, G., Gordon, C.T., Guo, Z., Jeong, J., Lee, W., Li, Z., Luo, L., Malyshev, S., Merryfield, W.J., Seneviratne, S.I., Stanelle, T., van den Hurk, B.J.J.M., Vitart, F., Wood, E.F., 2011. The second phase of the global land-atmosphere coupling experiment: soil moisture contributions to subseasonal forecast skill. J. Hydrometeorol. 12, 805–822. https://doi.org/10.1175/2011JHM1365.1.

Li, K., Zhang, J., Wu, L., 2018. Assessment of soil moisture-temperature feedbacks with the CCSM-WRF model system over East Asia. J. Geophys. Res.-Atmos. 123, 6822–6839. https://doi.org/10.1029/2017JD028202.

Li, Q., Wang, T., Wang, F., Liang, X.-Z., Zhao, C., Dong, L., Zhao, C., Xie, B., 2020. Dynamical downscaling simulation of the East Asian summer monsoon in a regional Climate-Weather Research and forecasting model. Int. J. Climatol. 41 (Suppl.1), E1700–E1716. https://doi.org/10.1002/joc.6800.

Liang, X.-Z., Kunkel, K.E., Samel, A.N., 2001. Development of a regional climate model for U.S. Midwest applications. Part I: sensitivity to buffer zone treatment. J. Clim. 14, 4363–4378. https://doi.org/10.1175/1520-0442(2001)014<4363:DOARCM>2.0.CO;2.

Liang, X.-Z., Xu, M., Choi, H.I., Kunkel, K.E., Rontu, L., Wang, J., 2005. Development of the regional Climate-Weather Research and forecasting Model (CWRF): Treatment of Subgrid Topography Effects. In: Preprints, Sixth WRF/15th MM5 Users' Workshop, Boulder, CO, NCAR, 9.3.

Liang, X.-Z., et al., 2012. Regional climate-weather research and forecasting model (CWRF). Bull. Am. Meteorol. Soc. 93 (9), 1363–1387. https://doi.org/10.1175/BAMS-D-11-00180.1.

Liang, X.-Z., Sun, C., Zheng, X., Dai, Y., Xu, M., Choi, H.I., Ling, T., Qiao, F., Kong, X., Bi, X., Song, L., Wang, F., 2018. CWRF performance at downscaling China climate characteristics. Clim. Dyn. 52, 2159–2184. https://doi.org/10.1007/s00382-018-4257-5.

Liang, X.-Z., Li, Q., Mei, H., Zeng, M., 2019. Multi-grid nesting ability to represent convections across the gray zone. J. Adv. Model. Earth Syst. 11, 4352–4376. https://doi.org/10.1029/2019MS001741.

Liu, S., Liang, X.-Z., Gao, W., 2008. Application of climate-weather research and forecasting model (CWRF) in China: domain optimization. J. Atmos. Sci. (in Chinese) 32 (3), 457–468. https://doi.org/10.3878/j.issn.1006-9895.2008.03.04.

Miralles, D.G., vanden Berg, M.J., Teuling, A.J., de Jue, R.A.M., 2012. Soil moisture-temperature coupling: a multiscale observational analysis. Geophys. Res. Lett. 39, L21707. https://doi.org/10.1029/2012GL053703.

Muñoz-Sabater, J., Dutra, E., Agustí-Panareda, A., Clément, A., Gabriele, A., Gianpaolo, B., Souhail, B., Margarita, C., Shaun, H., Hans, H., Brecht, M., Diego, G. M., María, P., Nemesio, J.R., Ervin, Z., Carlo, B., Jean-Noël, T., 2021. ERA5-Land: a state-of-the-art global reanalysis dataset for land applications. Earth Syst. Sci. Data. 13 (9), 4349–4383. https://doi.org/10.5194/essd-13-4349-2021.

Nevitt, J., Hancock, G.R., 2009. Performance of bootstrapping approaches to model test statistics and parameter standard error estimation in structural equation modeling. Struct. Eq. Model. Multidiscipl. J. 8 (3), 353–377. https://doi.org/10.1207/S15328007SEM0803_2.

Niu, G., Yang, Z., Mitchell, K.E., Chen, F., Ek, M.B., Barlage, M., Kumar, A., Manning, K. W., Niyogi, D., Rosero, E., Tewari, M., Xia, Y., 2011. The community NOAH land surface model with multiparameterization options (NOAH-MP): 1. Model description and evaluation with local-scale measurements. J. Geophys. Res.-Atmos. 116, D12109. https://doi.org/10.1029/2010JD015139.

Qiao, L., Zuo, Z., Zhang, R., Piao, S., Xiao, D., Zhang, K., 2023. Soil moisture–atmosphere coupling accelerates global warming. Nat. Commun. 14, 4908. https://doi.org/10.1038/s41467-023-40641-y.

Qing, Y., Wang, S., Yang, Z., Gentine, P., 2023. Soil moisture−atmosphere feedbacks have triggered the shifts from drought to pluvial conditions since 1980. Commun. Earth Environ. 4, 254. https://doi.org/10.1038/s43247-023-00922-2.

Santanello, J.A., Peters-Lidard, C.D., Kumar, S.V., 2011. Diagnosing the sensitivity of local land-atmosphere coupling via the soil moisture-boundary layer interaction. J. Hydrometeorol. 12, 766–786. https://doi.org/10.1175/JHM-D-10-05014.1.

Schaefli, B., van der Ent, R.J., Woods, R., Savenije, H.H.G., 2012. An analytical model for soil-atmosphere feedback. Hydrol. Earth Syst. Sci. 16, 1863–1878. https://doi.org/10.5194/hess-16-1863-2012.

Seneviratne, S., Lüthi, D., Litschi, M., Schär, C., 2006. Land–atmosphere coupling and climate change in Europe. Nature 443, 205–209. https://doi.org/10.1038/nature05095.

Seneviratne, S.I., Corti, T., Davin, E.L., Hirschi, M., Jaeger, E.B., Lehner, I., Orlowsky, B., Teuling, A.J., 2010. Investigating soil moisture-climate interactions in a changing climate: a review. Earth Sci. Rev. 99, 125–161. https://doi.org/10.1016/j.earscirev.2010.02.004.

Sun, C., Liang, X.-Z., 2020a. Improving US extreme precipitation simulation: sensitivity to physics parameterizations. Clim. Dyn. 54, 4891–4918. https://doi.org/10.1007/s00382-020-05267-6.

Sun, C., Liang, X.-Z., 2020b. Improving US extreme precipitation simulation: dependence on cumulus parameterization and underlying mechanism. Clim. Dyn. 55, 1325–1352. https://doi.org/10.1007/s00382-020-05328-w.

Wang, Z., Wu, R., Chen, Z., Zhu, L., Yang, K., Liu, K., Yang, Y., 2021. Decreasing influence of summer snow cover over the western Tibetan Plateau on East Asian precipitation under global warming. Front. Earth Sci. 9, 787971. https://doi.org/10.3389/feart.2021.787971.

Wei, F., 1999. Modern Climate Statistical Diagnosis and Prediction Techniques. China Meteorological Press.

Wei, J., Su, H., Yang, Z., 2016. Impact of moisture flux convergence and soil moisture on precipitation: a case study for the southern United States with implications for the globe. Clim. Dyn. 46, 467–481. https://doi.org/10.1007/s00382-015-2593-2.

Wei, J., Dirmeyer, P.A., Yang, Z., 2018. Effect of land model ensemble versus coupled model ensemble on the simulation of precipitation climatology and variability. Theor. Appl. Climatol. 134, 793–800. https://doi.org/10.1007/s00704-017-2310-7.

Wei, P., Dong, G., Shi, J., Zhang, B., 2019. Dynamical downscaling simulation and projection of extreme precipitation over East China. Clim. Res. (in Chinese) 24 (1), 86–104. https://doi.org/10.3878/j.issn.1006-9585.2018.17169.

Wei, J., Zhao, J., Chen, H., Liang, X.-Z., 2021. Coupling between land surface fluxes and lifting condensation level: mechanisms and sensitivity to model physics parameterizations. J. Geophys. Res.-Atmos. 126, e2020JD034313. https://doi.org/10.1029/2020JD034313.

Wu, J., Gao, X., 2013. A gridded daily observation dataset over China region and comparison with the other datasets. Chin. J. Geophys. 56 (4), 1102–1111. https://doi.org/10.6038/cjg20130406.

Xue, C., Shen, X., Ding, Z., Wu, N., Zhang, Y., Chen, X., Guo, C., 2022. Organizational modes of spring and summer convective storms and associated severe weather over Southern China during 2015–19. Mon. Weather Rev. 150 (11), 3031–3049. https://doi.org/10.1175/MWR-D-22-0061.1.

Yang, B., Zhang, Y., Qian, Y., Huang, A., Yan, H., 2015. Calibration of a convective parameterization scheme in the WRF model and its impact on the simulation of East Asian summer monsoon precipitation. Clim. Dyn. 44, 1661–1684. https://doi.org/10.1007/s00382-014-2118-4.

Yang, Y., Roderick, M.L., Guo, H., Diego, G.M., Lu, Z., Simone, F., Luo, X., Zhang, Y., McVicar, T.R., Tu, Z., Keenan, T.F., Fisher, J.B., Gan, R., Zhang, X., Piao, S., Zhang, B., Yang, D., 2023. Evapotranspiration on a greening Earth. Nat. Rev. Earth Environ. 4, 626–641. https://doi.org/10.1038/s43017-023-00464-3.

Yao, Y., Luo, Y., Huang, J., Ma, J., 2021. Improving the downscaled springtime temperature in Central Asia through assimilating meteorological and snow cover observations. Atmos. Res. 258, 105619. https://doi.org/10.1016/j.atmosres.2021.105619.

Yuan, X., Liang, X.-Z., 2011. Evaluation of a conjunctive surface–subsurface process model (CSSP) over the contiguous United States at regional–local scales. J. Hydrometeorol. 12, 579–599. https://doi.org/10.1175/2010JHM1302.1.

Zhang, X., Alexander, L.V., Hegerl, G.C., Jones, P.D., Tank, A.M., Peterson, T.C., Trewin, B., Zwiers, F.W., 2011a. Indices for monitoring changes in extremes based on daily temperature and precipitation data. Wiley Interdiscip. Rev. Clim. Chang. 2, 851–870. https://doi.org/10.1002/wcc.147.

Zhang, J., Wu, L., Dong, W., 2011b. Land-atmosphere coupling and summer climate variability over East Asia. J. Geophys. Res.-Atmos. 116, D05117. https://doi.org/10.1029/2010JD014714.

Zhang, Q., Zheng, Y., Singh, V.P., Luo, M., Xie, Z., 2017. Summer extreme precipitation in eastern China: Mechanisms and impacts. J. Geophys. Res.-Atmos. 122, 2766–2778. https://doi.org/10.1002/2016JD025913.

Zhang, Q., Gu, X., Li, J., Shi, P., Singh, V.P., 2018. The impact of tropical cyclones on extreme precipitation over coastal and inland areas of China and its association to ENSO. J. Clim. 31, 1865–1880. https://doi.org/10.1175/JCLI-D-17-0474.1.

Zhang, S., Wang, M., Wang, L., Liang, X.-Z., Sun, C., Li, Q., 2023. Sensitivity of the simulation of extreme precipitation events in China to different cumulus parameterization schemes and the underlying mechanisms. Atmos. Res. 285, 106636. https://doi.org/10.1016/j.atmosres.2023.106636.

Zhang, J., Li, C., Zhang, X., Zhao, T., 2024. Improving simulations of extreme precipitation events in China by the CMIP6 global climate models through statistical downscaling. Atmos. Res. https://doi.org/10.1016/j.atmosres.2024.107344.

Zhao, Y., Liang, X.-Z., 2024. Enhancing summer extreme precipitation prediction in the Yangtze River Basin through CWRF downscaling and its skillful multi-physics ensemble approach. Clim. Dyn. https://doi.org/10.1007/s00382-024-07153-x.

Zhao, Y., Qiao, F., Liang, X.-Z., Yu, J., 2024. Understanding and improving Yangtze River Basin summer precipitation prediction using an optimal multi-physics ensemble. Front. Earth Sci. 18 (1), 256–257. https://doi.org/10.1007/s11707-024-1118-x.

Zhu, H., Jiang, Z., Li, J., Li, W., Sun, C., Li, L., 2020. Does CMIP6 inspire more confidence in simulating climate extremes over China? Adv. Atmos. Sci. 37 (10), 1119–1132. https://doi.org/10.1007/s00376-020-9289-1.

Zou, L., Zhou, T., 2013. Near future (2016-40) summer precipitation changes over China as projected by a regional climate model (RCM) under the RCP8.5 emissions scenario: Comparison between RCM downscaling and the driving GCM. Adv. Atmos. Sci. 30, 806–818. https://doi.org/10.1007/s00376-013-2209-x.